Food Hydrocolloids 140 (2023) 108663

Contents lists available at ScienceDirect

Food Hydrocolloids

journal homepage: www.elsevier.com/locate/foodhyd

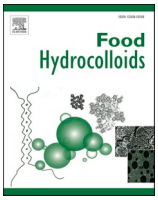

A microfluidic study of bubble formation and coalescence tuned by dynamic adsorption of SDS and proteins

Boxin Deng *, Karin Schroën, Jolet de Ruiter

Wageningen University, Food Process Engineering Group, Bornse Weilanden 9, 6708 WG, Wageningen, the Netherlands

ARTICLE INFO

Keywords:
Microfluidics
(sub)millisecond
Emulsifier adsorption
Dynamic surface tension
Bubble formation
Bubble coalescence

ABSTRACT

During foaming, bubbles are formed at *(sub)millisecond* time scales, and emulsifier adsorption determines bubble formation and stabilisation against coalescence. Here we introduce a microfluidic device, in which bubbles are formed in two distinct pressure regimes at low versus high pressures, and emulsifier adsorption can be inferred from the easily-monitored dynamics of bubble formation and coalescence, as well as the bubble properties. We studied dynamic adsorption for various types and concentrations of emulsifiers, namely sodium dodecyl sulfate (SDS; 0.05–3% wt.) and various proteins (5% wt.) including whey protein isolate (WPI), β-lactoglobulin (β-lac), and bovine serum albumin (BSA). The results show that as SDS concentration increases up to 3% wt., the *bubble formation time* decreases in the low-pressure regime due to the enhanced adsorption of SDS, yet increases in the high-pressure regime due to the promoted 'dripping-jetting' transition; in both pressure regimes the *neck thinning process* slows down, leading to longer bubble growth time and thus larger bubble size. To suppress coalescence of bubbles formed at time scales down to 10 μs, SDS is the most efficient, followed by BSA, WPI, and finally, β-lac; this is ascribed to the dynamics of emulsifier adsorption, e.g., the resulting dynamic surface tension. To conclude, our microfluidic study highlights the dynamic effects in the presence of SDS and proteins during bubble formation, even at high concentrations. This means that to explain the properties of a freshly-formed foam product, it is crucial to understand (and thereafter manipulate) emulsifier adsorption at time scales relevant to bubble formation and coalescence.

1. Introduction

Foams and emulsions are dispersions of two (semi-)immiscible phases that are typically stabilised with surface active components, i.e., emulsifiers. Emulsifier adsorption affects the interface in two ways, by lowering the interfacial tension and varying the interfacial rheological properties (e.g., viscous and elastic properties) (Joseph F., 1997; Tadros, 2013). At first, it promotes the formation of individual bubbles (and droplets) and determines their (initial) properties such as bubble formation frequency and size (Deng, Schroën, & De Ruiter, 2021), and at second, it hinders bubble coalescence and slows down the increase of bubble size with time (Jafari, Assadpoor, He, & Bhandari, 2008). Depending on the relative magnitude of time scales for bubble formation and emulsifier mass transfer, the surface tension of a freshly-formed bubble varies with time, known as *dynamic surface tension* (Walstra, Wouters, & Geurts, 2005; Zhu & Wang, 2017); therefore, bubble coalescence occurs upon collision if the bubble surface is insufficiently covered. Typically, emulsifier *type* and *concentration* can be manipulated to tune the relative magnitude of the above-mentioned time scales and thus bubble properties, and to do so, it is crucial to understand the emulsifier adsorption behaviour at time scales of bubble formation and coalescence. It is already good to point out that these time scales are very short and thus difficult to assess.

Microfluidics have been explored widely in making uniform droplets and bubbles, and also in unravelling dynamic processes occurring during the formation and stabilisation of droplets and bubbles, such as dynamic interfacial tension (Kalli, Chagot, & Angeli, 2022; Liang, Li, Wang, & Luo, 2022; Muijlwijk, Hinderink, Ershov, Berton-Carabin, & Schroën, 2016; Wang, Zhang, Zhang, & Luo, 2016; Xu, Dong, Zhao, Tostado, & Luo, 2012). Compared to conventional techniques – a pendant drop tensiometer that characterises emulsifier adsorption through measurement of dynamic interfacial tension and interfacial rheology for millimetre-sized interfaces at (lower than) second time scales (Berry, Neeson, Dagastine, Chan, & Tabor, 2015; Dabestani, Yeganehzad, Krzan, & Miller, 2019) –, microfluidic measurements provide direct insights into the roles of emulsifier adsorption at the

* Corresponding author.
E-mail address: boxin.deng@wur.nl (B. Deng).

https://doi.org/10.1016/j.foodhyd.2023.108663
Received 22 October 2022; Received in revised form 26 February 2023; Accepted 6 March 2023
Available online 12 March 2023

relevant *interfaces* (e.g., strongly curved) and *(sub)millisecond time scales*, as well as under the relevant *flow conditions* (Chen, Narayan, & Dutcher, 2020) Among the existing microfluidic devices, our partitioned Edge-based Droplet GEneration (partitioned-EDGE) microfluidic device stands out because of its capacity of forming and characterising monodisperse bubbles within two distinct pressure regimes, namely a low- and a high-pressure regime (Deng et al., 2021). This means that the partitioned-EDGE device can be used to study the roles of emulsifier adsorption both in lowering the (dynamic) surface tension leading up to bubble formation (Deng, Schroën, & De Ruiter, 2022) as well as in stabilising the formed bubble surfaces (Deng, Schroën, & De Ruiter, 2023), respectively.

The partitioned-EDGE device can characterise not only 'slow' emulsifiers such as whey protein isolate (as in our studies referenced above), but also 'fast' ones such as low-molecular weight surfactants; and it can be operated for both air-water (bubbles) and oil-water (droplets) systems. In the current study, we use the partitioned-EDGE system to study emulsifier adsorption in terms of its roles in dynamics of bubble formation and stabilisation against coalescence for various *types* and *concentrations* of emulsifiers. The monitored parameters are the bubble formation time that reflects the *dynamic surface tension*, as well as the bubble necking time and the neck thinning rate, which are influenced by both dynamic surface tension and interfacial rheology, in the low-pressure regime; while in the high-pressure regime, *the extent of bubble coalescence* is monitored and linked to the bubble formation time (i.e., the dynamic surfae tension). The results are discussed for a range of sodium dodecyl sulfate (SDS) concentrations (Section 3.2), and then compared between SDS and whey protein isolate (WPI; Section 3.3) and among SDS, WPI and other proteins (Section 3.4). We demonstrate that even for fast-adsorbing low-molecular weight surfactants, like SDS, dynamic effects are observed as function of surfactant concentration and applied pressure – effects that have been largely ignored in most microfluidic studies (Crestel, Derzsi, Bartolomei, Bibette, & Bremond, 2019; Mi, Fu, Zhu, Jiang, & Ma, 2019; Stoffel et al., 2012; Sugiura, Nakajima, Iwamoto, & Seki, 2001; Van Dijke, Schroën, van der Padt, & Boom, 2010) that operated under high surfactant concentrations in order to assume constant (equilibrium) interfacial tension in the production of droplets and bubbles.

2. Materials and methods

2.1. Materials

Air was used as the dispersed phase. Aqueous solutions (MilliQ, Merck Millipore) of emulsifiers were used as the continuous phase. The solutions used are 0.05, 0.1, 0.2, 0.5, 1, and 3% wt. sodium dodecyl sulfate (SDS; with >99% purity, Sigma-Aldrich, USA), 1% wt. Tween 20 (with >99% purity, Sigma-Aldrich, USA), and 5% wt. proteins, including whey protein isolate (WPI; with >97.5% purity, BiPro, Agropur, Canada), β-lactoglobulin (β-lac; with >95% purity, obtained by selective precipitation of commercial whey protein isolate), and bovine serum albumin (BSA; with ≥96% purity, Sigma-Aldrich, Germany). The pH of the protein solutions was approximately 7 (Sahin, Bliznyuk, Rovalino Cordova, & Schroën, 2016), and no adjustment was made in this study. All solutions were filtered with 0.22 μm PES filters (Merck, Germany) before use in the experiments. Filtration of protein solutions did not change their viscosity, and thus loss of protein was assumed to be negligible.

2.2. Partitioned-EDGE microfluidic chip

The custom-designed partitioned-EDGE microchips are made of borosilicate glass and produced by Micronit Microtechnologies B.V. (Enschede, the Netherlands). The geometry consists of two deep channels, with one straight channel for the dispersed phase and one meandering channel for the continuous phase (Fig. 1A). The deep channels are connected by a shallow plateau (green box) of 200 μm length (L) and 500 μm width (W). The shallow plateau is further partitioned into eight identical parallel pores with 20 μm length (l) and 40 μm width (w) on the continuous phase side (Fig. 1B). Unless stated otherwise, the main plateau and pores have 1 μm height (h). In the experiment, the chip is put in a chip holder (Fluidic Connect 4515, Micronit Microfluidics) and connected to the dispersed and continuous phases using PEEK tubing (0.75 mm, BGB®, Switzerland); with the outlet being closed, the pressurised dispersed phase flows continuously onto the main plateau and pores, and finally into the continuous phase in the form of bubbles. Here, the partitioned-EDGE device was used to study bubble formation (Fig. 1C) and coalescence (Fig. 1D).

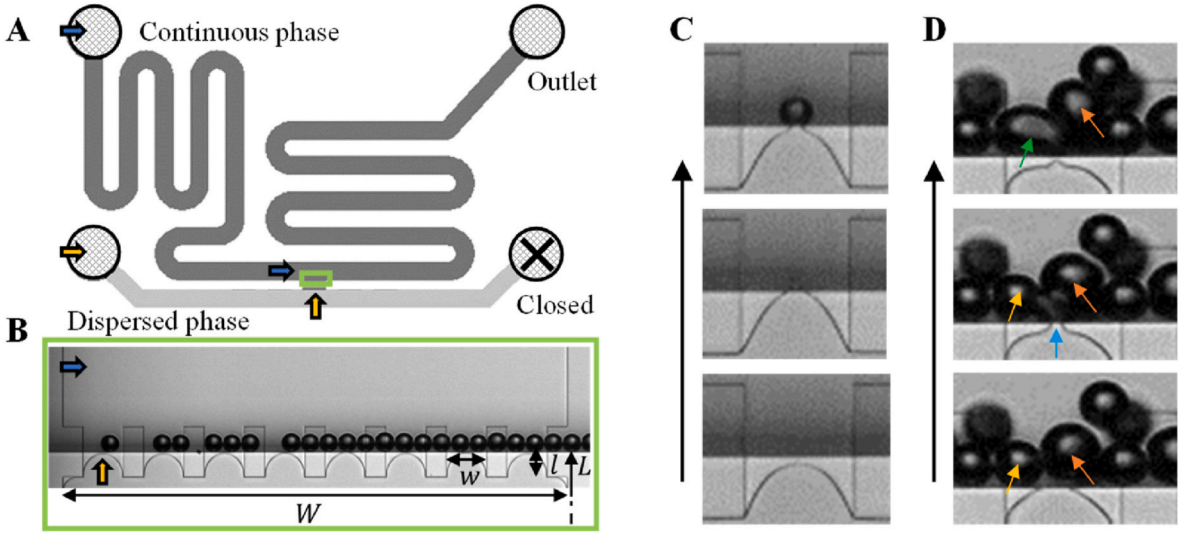

Fig. 1. Layout of the partitioned-EDGE device (A) and the pores on the continuous phase side of the shallow plateau (B). C. One bubble formation cycle. From bottom to top: the meniscus moves towards and leaps over the edge of the pore, leading to a growing bulb. D. Bubble formation and coalescence at the pore; coalescence of the two bubbles marked by ↗ and ↗ leads to the formation of the bubble marked by ↗. Bubbles are stabilised either immediately after formation or after coalescing a few times (↗). In C and D, the bottom-to-top arrows indicate time.

2.3. Microfluidic experiments

Both air and continuous phases were pressurised using a digital pressure controller (Elveflow®, Paris, France), which controls pressures at an accuracy below 0.1 mbar, via Smart Interface Software (Elveflow®, France). In the experiment, air is firstly pressurised at P_d and the continuous phase is then pressurised at P_c, resulting in a pressure difference across the main plateau and pores (Deng et al., 2021), namely the applied pressure $P_d^* = P_d - P_c/2$. While P_d^* is varied, the continuous phase velocity (v_c) is kept constant in each pressure regime to avoid any effect of shear, namely approximately 0.1 m/s in the low-pressure regime and 1 m/s in the high-pressure regime. Lastly, it is worth to mention that in the experiments with SDS, the microchip was pretreated with 5% wt. WPI (which would form a more hydrophilic layer, following a proven method (Sahin et al., 2016)) to avoid retraction of the meniscus at low SDS concentrations and applied pressures.

2.4. Data analysis

Videos and images were recorded using a high-speed camera (FASTCAM SA-Z, Photron Limited, Japan) that is connected to the microscope (Axiovert 200 MAT, Carl Zeiss B·V., the Netherlands). In each experiment, two videos were recorded. One is recorded at a frame rate of 700,000 fps for the characterisation of time scales, including bubble necking time (t_n) and pore filling time (t_{fill}). t_n was obtained by counting the number of frames, through which the neck thinning process proceeded, and t_{fill} represents the lag time between two subsequent neck thinning processes. The bubble formation time (τ) is $\tau = t_{fill} + t_n$. The other video is recorded at a frame rate of 100,000 fps for the measurement of bubble sizes. A custom-written script in Matlab R2018b was used for the analysis of bubble sizes. The initial bubble size, d_0, was averaged for up to 50 bubbles; and the coalesced bubble size, d_{coal}, was averaged for up to 100 bubbles. The coefficient of variation, CV (%) = $(\sigma/d) \times 100$ (with σ the standard deviation and d the number-averaged diameter) was calculated to describe the bubble size distribution.

3. Results and discussion

3.1. Background: roles of dynamic adsorption in the partitioned-EDGE device

In an earlier study of bubble formation in the partitioned-EDGE device, whey protein isolate was used as the emulsifier, and bubble formation shows a low- and a high-pressure regimes, delineated by the Laplace pressure of the meniscus devoid of any emulsifier (P_{tran}) (Fig. 2A) (Deng et al., 2021). The two pressure regimes are further bounded by, on the low side, the *breakthrough pressure* (P_{min}), which is the Laplace pressure of the meniscus saturated with emulsifiers, and on the high side, the *cross-over pressure* (P_{cross}) that will be discussed below.

The transition and breakthrough pressures can be calculated using the Young-Laplace equation $\Delta P_L = \gamma\left(\frac{1}{R_1} + \frac{1}{R_2}\right)\cos(\theta)$, where R_1 and R_2 are the principal radii of curvature, γ the surface tension, and θ the contact angle between the channel wall and the continuous phase.

One bubble formation cycle is divided into two stages: the pore filling stage and the bubble necking stage. In the low-pressure regime ($P_d^* < P_{tran}$), *the meniscus* requires protein adsorption to lower its *surface tension* and thus the Laplace pressure below the applied pressure. The pore filling stage consists of not only this adsorption process (at position 1 in Fig. 2B), which is slow, but also a subsequent pore flow that is initiated as soon as $\Delta P_L \leq P_d^*$ and much faster (than the adsorption process). During the pore flow, the meniscus moves forward inside the pore until it reaches the edge of the pore (position 1 to 2, Fig. 2B). The pore filling time (t_{fill}) is determined by the applied pressure and protein adsorption. Afterwards, in the bubble necking stage, the (partially-) covered meniscus leaps over the edge and expands outside the pore (position 2 to 3, Fig. 2B) into a bulb that grows in volume while the neck narrows, and the neck finally quickly snaps off when its width is below the pore's height (indicated by shape 4 in Fig. 2B). The necking time (t_n) is much shorter than the filling time ($t_{fill} \gg t_n$). In the high-pressure regime with $P_d^* > P_{tran}$, the pore flow immediately takes place without prior protein adsorption, driven by a positive pressure drop of $P_d^* - P_{tran}$, and the t_{fill} decreases as function of the applied pressure and converges to t_n (Fig. 2C). The neck width narrows faster in the high-pressure regime than in the low-pressure regime, resulting in shorter t_n, which was ascribed to the continuous phase inflow (Deng et al., 2022). The pressure at which the filling time and the necking time intersect is defined as P_{cross}, and above this pressure the 'dripping-jetting' transition can occur, which leads to increased bubble size and polydispersity (Deng et al., 2022). Thus, the P_{cross} bounds the well-defined high-pressure regime.

Bubble formation and thus bubble properties show distinct dependencies on dynamic adsorption in the two pressure regimes (Deng et al., 2021). In the low-pressure regime, protein adsorption plays an important role in the initiation of bubble formation and thus the bubble formation frequency. Next to that, protein adsorption at the meniscus influences the interfacial properties of the meniscus, and thus the necking time t_n and ultimately, the initial bubble size d_0. These initial bubbles are formed at an extremely low frequency (i.e., typically below tens of bubbles per second) and stabilised before the occurrence of bubble-bubble collision that may induce coalescence. In contrast, in the high-pressure regime, these initial bubbles form and coalesce immediately, leading to large bubbles with size d_{coal} (Fig. 2A). The extent of bubble coalescence can be reduced by decreasing the bubble formation frequency (i.e., decreasing P_d^*) and stabilising the bubble surfaces (e.g., via increasing the protein concentration).

In the current work, *dynamic adsorption* is studied for various types (i.e., SDS and proteins) and concentrations of emulsifiers. First, the

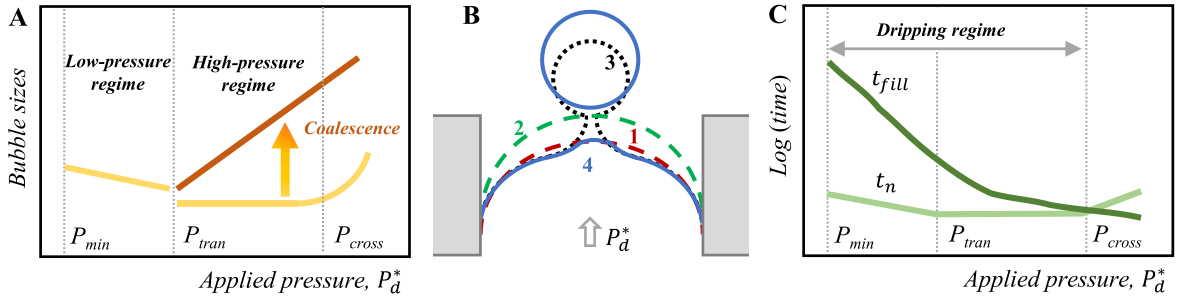

Fig. 2. Schematic illustration of bubble formation and coalescence behaviours in the partitioned-EDGE device. A. Division of low- and high-pressure regimes, and the three crucial pressures, in the presence of whey protein. Light yellow line represents d_0 and orange line represents d_{coal}. B. One bubble formation cycle (1–4): 1 – backmost position of meniscus inside the pore; 2 – initiation of necking; 3 – necking and bubble growth; 4 – neck break-up. C. The filling time (t_{fill}: 1 → 2 in B) and necking time (2 → 4 in B) as function of the applied pressure.

formation and coalescence of bubbles stabilised with a standard low-molecular weight surfactant, SDS is described (Section 3.2); second, the results obtained for SDS are qualitatively compared with those obtained for WPI (Section 3.3) that has been described in previous work (Deng et al., 2022), and further with those obtained for β-lac and BSA (Section 3.4). This work allows us to highlight emulsifier-related kinetics during the highly dynamic processes that underlay foaming, even for 'fast' adsorbing low molecular weight surfactants such as SDS.

3.2. Bubble formation and coalescence: SDS concentration effects

3.2.1. The bubble formation time

The formation time (τ) of SDS-stabilised bubbles is plotted as function of the applied pressure in Fig. 3. In the low-pressure regime below 1400 mbar, $t_{fill} \gg t_n$ and thus $\tau \approx t_{fill}$. τ decreases monotonically as function of P_d^* since at increasing applied pressure, an increasingly higher surface tension already enables the pore flow to occur and thus shortens the lag time resulted from SDS adsorption. In addition, τ decreases as SDS concentration increases up to 3% wt., due to the faster adsorption and thus the faster reduction in the surface tension (Deng, Schroën, Steegmans, et al., 2022). For SDS concentrations above the critical micelle concentration, which is approximately 0.20–0.28% wt. (Kinoshita, Parra, & Needham, 2017; Liang et al., 2022; Sugiura et al., 2001; Wang, Riaud, Wang, & Luo, 2015; Xu et al., 2012), mass transfer is enhanced due to the higher number density of SDS monomers resulting from fast disaggregation of SDS micelles (Wang et al., 2009, 2015; Xu et al., 2012). In the high-pressure regime, τ eventually increases with P_d^*, and this is a function of SDS concentration. For 0.05–0.1% wt. SDS, τ decreases as P_d^* is raised up to 1800 mbar, and afterwards increases slightly. For 0.2–0.5% wt. SDS, τ jumps from 0.02 to 0.1 ms at 1800 mbar, and then levels off. For 1–3% wt. SDS, the shortest τ is obtained at about 1500 mbar, and thereafter, τ slightly increases with P_d^* and levels off since 1800 mbar. It should be noted that in the high-pressure regime, t_{fill} decreases with the applied pressure, showing no dependency on the SDS concentration (Fig. A1). This indicates that any decrease in surface tension of the meniscus (and thus its Laplace pressure) due to SDS adsorption during the pore filling stage is negligible, and the decrease of the pore filling time is exclusively due to the higher driving pressure – the higher applied pressure. As will be discussed below, the bubble necking time largely dominates the strongly shortened pore filling time at high applied pressures, leading to the observed increase of overall bubble formation time around 1800 mbar in Fig. 3.

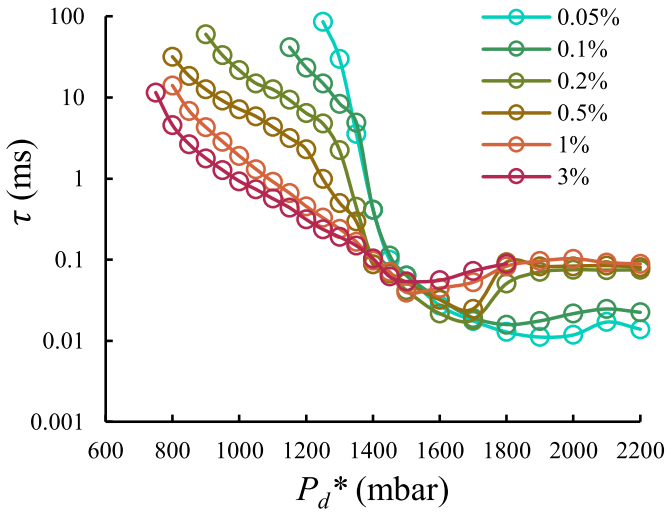

Fig. 3. The bubble formation time as function of the applied pressure for a range of SDS concentrations. The transition pressure is 1400 mbar.

3.2.2. The bubble necking time

The influence of SDS concentration was also evaluated for the bubble necking time (t_n). t_n is a result of the neck thinning process, which is influenced by the interfacial properties of the meniscus. Across the full range of applied pressures, irrespective of the pressure regime (i.e., P_{tran} = 1400 mbar), t_n varies in three sub-ranges (Fig. 4A), divided as follows: I. the plateau phase at $P_d^* \leq$1150 mbar; II. bubble formation in the dripping regime for *all* SDS concentrations at 1150 < $P_d^* \leq$1500 mbar (with the upper bound being given by the lowest P_{cross} for the used SDS concentrations, namely 1550 mbar for 3% wt.); III the start of bubble polydispersity at P_d^* >1500 mbar (induced first for the highest SDS concentration). The sub-range I exists only for SDS concentrations above 0.2% wt., and in this sub-range, t_n remains constant as function of P_d^* and increases with SDS concentration. We looked into the neck thinning process and observed that the neck thinning rate is independent of the applied pressure (Fig. A2A), while it is lower as SDS concentration increases, which was also observed in previous study (Kovalchuk, Nowak, & Simmons, 2016). In sub-range II, t_n decreases as function of P_d^*, and this is a function of SDS concentration. For 0.05–0.2% wt. SDS, this is due to an overall faster necking process (Fig. A2B), accelerated by the increasing dynamic surface tension at the neck region with increasing P_d^* (Kovalchuk, Nowak, & Simmons, 2017). For 0.5–3% wt. SDS, the neck thinning rate varies with time; there is a strong increase in the thinning rate with applied pressure at the beginning of the thinning process, but within 5 μs all thinning rates again reduce to the low-pressure value (Fig. A2C). The shift in thinning rate likely indicates a sudden decrease of the initially-higher surface tension at the neck region due to the faster replenishment of SDS monomers from the continuous phase inside the pore, or a Marangoni flow along the expanding bubble surface towards the neck region (Roché, Aytouna, Bonn, & Kellay, 2009). Lastly, in sub-range III, t_n again increases significantly as function of P_d^* – which explains the increase in τ as shown in Fig. 3. The increase of t_n starts at P_{cross} that decreases from 1750 mbar for 0.05% wt. SDS to 1550 mbar for 3% wt. SDS. This is in line with the initiation of dripping-jetting transition at P_{cross} (Deng et al., 2022), which occurs earlier for lower interfacial tension (Sugiura, Nakajima, Oda, Satake, & Seki, 2004).

3.2.3. The size of initial and coalesced bubbles

Depending on the applied pressure and SDS concentration, initial bubbles of size d_0 may further coalesce, leading to enlarged bubbles of size d_{coal}. In sub-range I (Fig. 4B), the bubble size is d_0, and it increases almost linearly as function of P_d^*. This can be ascribed exclusively to an increase in the air flow rate into the growing bubble (Q'_{bub}), since the bubble volume is linear in both the air flow rate and the necking time ($V_0 = Q'_{bub} \times t_n$), and the latter remains relatively constant (Fig. 4A). In sub-range II up to 1350 mbar, d_0 decreases as function of P_d^* because of the strong decrease of t_n (Fig. 4A) that dominates the continuously increasing Q'_{bub}. Typically, in the low-pressure regime (e.g., at $P_d^* \leq$ 1350 mbar), initial bubbles are formed and stabilised before the occurrence of bubble-bubble collision that may lead to bubble coalescence. The d_0 increases for SDS concentrations above 0.2% wt., which is in line with the changes in t_n.

At the higher applied pressures in sub-range II, the bubble size shows distinct variations as function of P_d^* in the range of 1400 $\leq P_d^* \leq$ 1500 mbar for different SDS concentrations. Firstly, for c = 0.05% wt., bubble coalescence is observed since P_d^* = 1450 mbar, which is responsible for the marked increase in bubble size (inset of Fig. 4B). Secondly, for c > 0.2% wt., d_0 continuously decreases as P_d^* increases to up to the end of sub-range II (and increases with SDS concentration). Thirdly, for intermediate concentrations, like c = 0.1–0.2% wt., bubble coalescence is likely partly suppressed; the bubble size remains constant at approximately 17 μm and is independent of the applied pressure and SDS concentration. The constant bubble size is likely because that the few coalescence events balance out the decrease in d_0. In sub-range III, the

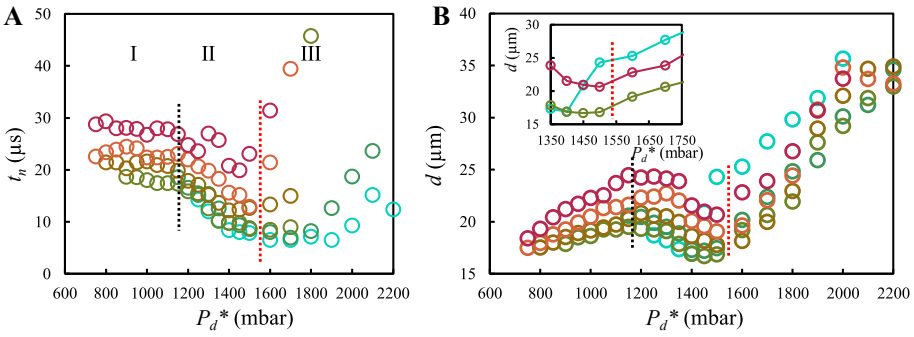

Fig. 4. A. Effects of SDS concentration on the bubble necking time as function of the applied pressure for 0.05 (○), 0.1 (○), 0.2 (○), 0.5 (○), 1 (○) and 3% (○) wt. SDS. The bubble necking times above 50 μs (for SDS concentrations ≥0.2% wt.) have been excluded here; at high applied pressures, they level off at a value that slightly increases with SDS concentration as can be seen in Fig. 3 ($t_n \approx \tau$). B. The corresponding bubble size as function of the applied pressure for the same range of SDS concentrations. Dashed lines: the transition between I and II (black) or II and III (red). Inset: highlight of the difference for 0.05, 0.2 and 3% wt. at the transition between II and III.

bubble size shows an overall increasing trend with the applied pressure. The bubble size is influenced by multiple aspects, such as the initial bubble size, the extent of bubble coalescence and the dripping-jetting transition. As a result, the bubble size shows a non-monotonous behaviour as function of the SDS concentration, leading to polydispersity.

Typically, although the dripping-jetting transition occurs at lower applied pressure as SDS concentration increases, the dripping regime is still wider, due to the larger impact of increasing SDS concentration on the initiation of bubble formation. Accordingly, the dripping regime widens and shifts to lower applied pressures. In the low-pressure regime, bubbles are mostly monodisperse with CV around 5% (Fig. A4); in the high-pressure regime, bubbles become much more polydisperse due to the finite extent of bubble coalescence, and most importantly, the formation of polydisperse, large bubbles upon dripping-jetting transition.

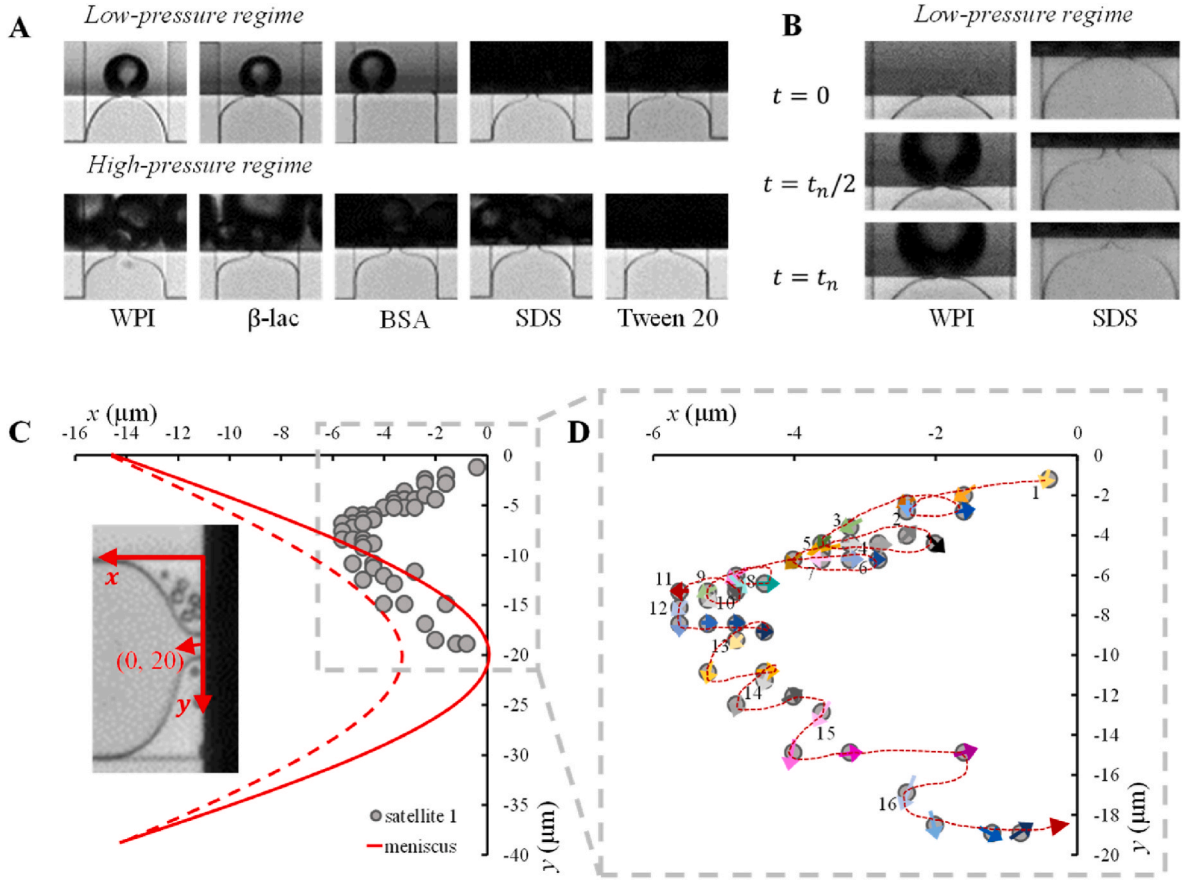

Fig. 5. A. Snapshots recorded in the middle of a necking process at 1250 (up) and 1700 (bottom) mbar, respectively, for a range of emulsifiers. B. The comparison of necking behaviour in the presence of WPI and SDS in the low-pressure regime. C. The time-dependent positions of one satellite bubble (grey circles) inside the pore, observed at $P_d^* = 1350$ mbar for 3% wt. SDS. The positions were analysed every 20 μs. The red solid and dashed lines represent the positions of the meniscus when the neck starts thinning and breaks up, respectively. Inset: Multiple satellite bubbles inside the pore. D. The instantaneous moving directions of one satellite bubble along its trajectory. The numbers (1–16) indicate a sudden change in the moving direction of the satellite bubble; for each number the colour gradient (light to dark) indicates time (not drawn to scale to represent velocity). The dashed line is drawn to guide the eye.

3.3. Comparison between SDS and WPI

3.3.1. Critical pressures

While the transition pressure (P_{tran}) is solely determined by the device geometry and dimension, the type of interface (e.g., air-liquid or liquid-liquid), and also the contact angle between the continuous phase and the channel wall (Deng et al., 2022), both the breakthrough pressure (P_{min}) and the cross-over pressure (P_{cross}) show dependencies on the type and concentration of emulsifiers. As an illustration, at a constant transition pressure (i.e., 1400 mbar in this study), P_{cross} decreases from approximately 1750 to 1550 mbar as SDS concentration increases from 0.05 to 3% wt., and it decreases from 1900 to 1700 mbar as WPI concentration increases from 2.5 to 10% wt. (Deng et al., 2022). This implies maybe counter-intuitively that high emulsifier concentrations are detrimental for controllable high-frequency production of *monodisperse, small* bubbles, even though bubbles are stabilised against coalescence to a higher extent. In practise, an 'optimal' concentration can be chosen such that bubbles are formed at a high frequency in the dripping regime, and are stabilised simultaneously and sufficiently.

3.3.2. Continuous phase inflow indicated by inflowed satellite bubbles

For SDS and WPI, we observed fundamental differences during bubble formation at the pore. The neck thinning process, leading to snap-off of a bubble, can be accompanied by continuous phase inflow (into the pore), which is driven by a pressure drop along the pore and into the continuous phase. For WPI, this inflow was observed only in the high-pressure regime, characterised by the formation of *long necks* (comparing the top and bottom rows of Fig. 5A for WPI) and the *back-and-forth movements* of the meniscus (inside the pore) during the consecutive cycles of bubble formation (Deng et al., 2022). In the low-pressure regime, the inflow is absent, and the neck is short (Fig. 5A). However, in the presence of SDS the continuous phase inflow exists in both pressure regimes, as illustrated by the difference in the necking behaviours for WPI and SDS in the low-pressure regime (Fig. 5B) and the similarities of the neck shape in both pressure regimes for SDS (Fig. 5A). Besides, the continuous phase inflow can be visualised by system-specific 'tracking-particles', namely satellite bubbles (Fig. 5C) originating from the necking process (see also Fig. A3). Along with the continuous phase, these satellite bubbles inside the pore are repeatedly accelerated and decelerated during the bubble necking stage and the subsequent pore filling stage (Fig. 5D), corresponding to the back-and-forth movements of the meniscus. In the partitioned-EDGE system, the satellite bubbles were observed at high emulsifier concentrations, for example in the presence of 3% wt. SDS and 20% wt. WPI. In contrast to the bubble system, satellite droplets (hexadecane-in-water) were observed for an extended range of SDS concentrations above 0.5% wt., which agrees with previous observations (Vladisavljevi, Kobayashi, & Nakajima, 2008). Hence, the formation of satellite bubbles (and droplets) can be ascribed to an effective decrease in surface tension at the neck region during the neck thinning process, on a time scale of a few microseconds (as discussed in Section 3.2.2 and Fig. A2). The extended range of SDS concentrations supporting satellite formation in the droplet system can be ascribed to the higher viscosity of hexadecane that prolongs the neck thinning process and thus allows more SDS molecules to adsorb at the neck region, which sufficiently lowers the interfacial tension even at low concentration SDS.

The distinct interfacial behaviours of WPI and SDS are likely responsible for the observed differences in necking behaviour. Proteins lower the interfacial tension more slowly upon adsorption and exhibit intermolecular interactions at the interface that endows the interface with viscoelasticity (Hinderink et al., 2021; Tcholakova, Denkov, & Lips, 2008). Besides, the interfacial tension starts to decrease only when the surface coverage exceeds 1 mg/m^2 of protein (De Jongh et al., 2004). According to Hinderink et al. (2021), intermolecular interactions between protein molecules signifying an early-stage interfacial network, are already present at time scales of 0.16–1 s. In the low-pressure regime for WPI, the bubble formation time is in the range of 0.01–1s; an (early-stage) interfacial network can be expected to modify the viscoelasticity of the meniscus, which becomes more viscous and less deformable. Therefore, during the necking process in the low-pressure regime, the meniscus experiences a higher resistance towards deformation, and is confined to the exit of the pore; while in the high-pressure regime, a much higher WPI (in comparison to SDS) concentration is required to produce satellite bubbles. SDS adsorption induces a faster decrease of surface tension without viscoelasticity, which allows for a deformable neck that stretches easily and supports satellite bubble formation. Lastly, the typical interfacial behaviour of WPI versus SDS is also seen for other emulsifiers (Fig. 5A): with two other proteins (e.g., 5% wt. β-lac and BSA), we see long necks and the back-and-forth movements of the meniscus only in the high-pressure regime, while with low-molecular weight surfactants (1% wt. SDS and Tween 20) we observe these characteristics in both pressure regimes.

3.4. Comparison among SDS, WPI and other proteins

3.4.1. Bubble formation dynamics

In this section, the results obtained for 5% wt. proteins, including WPI, β-lac, and BSA, were compared to those obtained for 0.1% wt. SDS. Due to the large difference in molecular properties of SDS and proteins, comparing the bubble formation behaviour at equal concentration, either weight or molar, would lead to vastly different bubble formation regimes. Here, the concentration of SDS is chosen as 0.1% wt., which is 1:50 in terms of weight concentration and only roughly 5:1 in terms of molar concentration. Most importantly, it was chosen to best match the general behaviour of the protein-stabilised bubbles in terms of both dynamic surface tension and stability against coalescence. Namely, 0.1% wt. SDS as compared to proteins shows similar trends in bubble necking time (Fig. 6A) and bubble formation time (Fig. 6B). This indicates a similar, although negligible, decrease of surface tension of the meniscus during the pore flow and the neck thinning process – even though SDS adsorption is overall faster as will be discussed below. At the same time, the range of applied pressures supporting stable bubble formation (via dripping) and a finite extent of bubble coalescence is bounded by a similar P_{cross} for proteins and relatively low concentrations of SDS. Hence, most comparisons will hold qualitatively if slightly different SDS concentration is chosen.

The bubble necking time as function of the normalised applied pressure is shown in Fig. 6A. In the low-pressure regime, t_n decreases as function of the normalised applied pressure – as previously shown for low concentrations of SDS and WPI (Deng et al., 2022). Compared to those of SDS, t_n values (and thus d_0 values shown in Fig. 6C) obtained for proteins are higher, which can be ascribed to interfacial viscoelasticity due to intermolecular interactions of adsorbed proteins (Narsimhan & Xiang, 2018). Among proteins, the slight difference observed in t_n and thus d_0, may reflect differences in the strength of interfacial network or of interaction between proteins and channel wall (Sahin et al., 2016). In the high-pressure regime at normalised applied pressures below 400 mbar, t_n values are independent of the applied pressure and the type of emulsifier, indicating that during the pore filling stage and the neck thinning process any adsorption towards the meniscus can be ignored. At higher normalised applied pressures, t_n starts increasing upon dripping-jetting transition, for first SDS and then BSA, while t_n levels off for WPI and β-lac (Fig. 6A). As illustrated for WPI (Deng et al., 2022) and SDS (Fig. 4A) at increasing concentrations, the sudden increase in t_n is likely resulting from combined effects of lowered pore filling time (decreasing below t_n) and (enhanced) emulsifier mass transfer from the expanding bubble surface towards the neck region. The latter describes the so-called Marangoni flow, which delays the final break-up of the neck (Giménez-Ribes, Sagis, & Habibi, 2020).

The bubble formation time is closely set by the initiation of bubble formation in the low-pressure regime, and sets the bubble coalescence stability in the high-pressure regime. In the low-pressure regime, τ

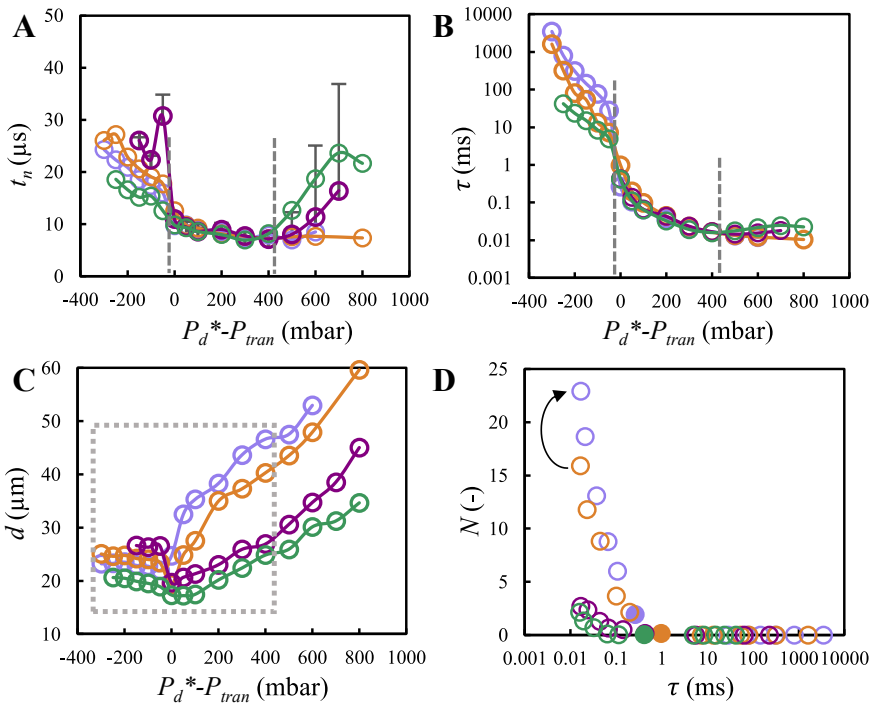

Fig. 6. The bubble necking time (A), the bubble formation time (B), and the bubble size (C) as function of the normalised applied pressure for 0.1% wt. SDS (○) and 5% wt. β-lac (○), WPI (○), and BSA (○). The proteins were tested in a chip with pore height of 0.93 µm, which leads to $P_{tran} = 1500$ mbar. To fairly compare the results, the normalised applied pressures of $(P_d^* - P_{tran})$ were calculated. D. The number of coalescence events as function of the bubble formation time. The transition pressure is marked with filled symbols for SDS and various proteins. In D, the arrow guides the eye: comparison between WPI and β-lac at certain τ. In the high-pressure regime, bubbles with $N < 0.5$ are considered stable.

strongly decreases as function of the normalised applied pressure, and SDS adsorption is more efficient than proteins (i.e., WPI followed by β-lac) in lowering the dynamic surface tension and thus initiating the bubble formation (e.g., a shorter bubble formation time, Fig. 6B). Here, besides the nature of distinct emulsifiers, one of the possible reasons explaining the shorter τ obtained for SDS is that SDS adsorption is likely enhanced due to continuous phase inflow, which creates a flow field and eddies in the continuous phase inside the pore and also refreshes the continuous phase timely. For proteins, the higher efficiency of WPI compared to β-lac was also found during emulsification studies; namely, upon emulsification at a comparable applied pressure, WPI yielded many more droplets than β-lac (Sahin et al., 2016). In the high-pressure regime, at normalised applied pressures below 400 mbar, τ decreases as function of the normalised applied pressure, showing again no dependency on the type of emulsifier. Here, τ is mainly determined by the applied pressure and the (almost constant) hydrodynamic flow resistance of the pore. At higher applied pressures, τ starts increasing mainly for SDS and BSA, which is in line with that observed for t_n (Fig. 6A).

3.4.2. *Bubble coalescence dynamics*

In the high-pressure regime, initial bubbles (with size d_0) further coalesce, and the coalesced bubble size (d_{coal}) increases as function of the normalised applied pressure (Fig. 6C). While the d_0 values are independent of the normalised applied pressure and the type of emulsifier in the high-pressure regime (Fig. A5), the d_{coal} values are smaller for SDS than for proteins, with the latter showing an order of BSA < WPI < β-lac (Fig. 6C). To compare the stabilising effects of emulsifier adsorption at the bubble surface, we further calculate the number N of coalescence events that a coalesced bubble has undergone. By using the volumes of initial ($V_0 = \frac{\pi}{6} d_0^3$) and coalesced bubbles ($V_{coal} = \frac{\pi}{6} d_{coal}^3$), the number of coalescence events, $N = \frac{V_{coal}}{V_0} - 1$, was calculated for normalised applied pressures that produce *initially monodisperse* bubbles (within the dashed box) and plotted as function of the bubble formation time. In Fig. 6D, as expected, bubbles are formed and immediately stabilised ($N = 0$) in the low-pressure regime at $\tau > 1$ ms for proteins and at $\tau > 0.1$ ms for SDS. In the high-pressure regime at τ being as low as 10 µs, the extent of bubble coalescence shows strong dependence on the type of emulsifier. N values are relatively identical for SDS and BSA, and they are much lower than those obtained for WPI followed by β-lac. Within *short-term*, BSA and, to a smaller extent, WPI are more efficient than β-lac in stabilising the initial and coalesced bubbles, which is in line with their ability to lower the *dynamic surface tension* as observed in the low-pressure regime. The change of surface tension is a function of protein structure, and here the observation that BSA reduces surface tension faster (than β-lac) can be ascribed to the larger surface area of BSA molecules, which (upon adsorption) reaches the critical surface coverage (i.e., 2/3 of the maximum possible coverage) that terminates the induction period and initiates the rapid fall (in surface tension), earlier (Gao & Rosen, 1995; Graham & Phillips, 1979). Therefore, the better foamability and short-term foam stability of WPI than β-lac likely results from its constitute(s) BSA (and α-lac (Sahin et al., 2016), which yielded many more droplets than WPI, as observed in previous emulsification study).

The short-term observation here is in stark contrast to the long-term observation obtained for a homogeniser. For example, at a constant concentration (2% wt., pH 7), the emulsifying capacity of these proteins is in the order of β-lac > BSA (Joseph F., 1997), which is in line with their ability to reach a lower *equilibrium interfacial tension* that is in the order of β-lac (< WPI) < BSA, obtained at a concentration up to 0.5% wt. (Saito, Yin, Kobayashi, & Nakajima, 2005; Mitropoulos, Mütze, & Fischer, 2014). Moreover, according to Muijlwijk, Colijn, Harsono, Krebs, and Berton-Carabin (2017), to stabilise droplets against coalescence, a *higher* concentration and a *longer* adsorption time are needed for WPI (100 ms for 0.01% wt. WPI) than for β-lac (31 ms for 0.005% wt. β-lac), which, maybe surprisingly, hints at poorer performance of WPI in their experiment. On one hand, it is important to realise that in the coalescence chamber used by Muijlwijk and co-authors, 100 ms and 31 ms are relatively long times, during which emulsifiers are allowed to adsorb at the interface of individual and spatially-separated droplets. It is reasonable that droplets can be stabilised with an extremely low

emulsifier concentration when the adsorption time is long enough to obtain monolayer surface coverage. On the other hand, to stabilise droplets and bubbles against coalescence on a *long-term*, not only fast adsorption (which could result in a fast decrease in dynamic interfacial tension and *short-term* stabilisation) is important, but also interactions between emulsifier molecules at the interface are crucial. Accordingly, more factors are likely playing a role in interface stabilisation; in terms of proteins, the factors can be the microstructure of the proteins, the formation of a viscoelastic interface, the purity of proteins adsorbed at the interface (Muijlwijk et al., 2017) and the oxidation level (Hinderink, Kaade, Sagis, Schroën, & Berton-Carabin, 2020) of the proteins, just to name a few.

4. Conclusions

An important feature of the *partitioned-EDGE* device is the extreme shallowness of the main plateau and pores, which introduces high Laplace pressures that dominate bubble formation. The Laplace pressure of the bare meniscus marks the transition between low- and high-pressure regimes of bubble formation. Emulsifier adsorption plays a role in the initiation of bubble formation (i.e., bubble formation frequency) in the low-pressure regime, and in the bubble stabilisation in the high-pressure regime. At tine scales relevant to bubble formation, these roles mainly depend on the efficiency of emulsifier adsorption in lowering the dynamic surface tension of the meniscus and the bubble surface, respectively. Next to that, in the low-pressure regime, emulsifier adsorption affects the interfacial rheological properties of the meniscus, which influence the neck thinning process and thus the initial bubble size.

Emulsifiers (i.e., SDS and proteins including WPI, β-lac, and BSA) were tested at various concentrations (i.e., 0.05–3% wt. for SDS and 5% wt. for proteins) in this work. As SDS concentration increases, the bubble formation frequency increases in the low-pressure regime due to the faster adsorption of SDS monomers, and decreases in the high-pressure regime due to the earlier dripping-jetting transition, upon which large initial bubbles are formed at the pores. In addition, we retrieved the fact that SDS adsorption is more efficient than that of proteins. Specifically, in the order of SDS, BSA, WPI and β-lac, emulsifier adsorption towards the meniscus (inside the pore) leads to an increasingly higher bubble formation frequency in the low-pressure regime, and that towards the bubble surface, at time scales down to 10 μs (i.e., short-term stabilisation), results in an increasingly lower extent of bubble coalescence in the high-pressure regime. Last but the least, the fact that the dynamic processes occurring during bubble formation and stabilisation can be assessed individually in the partitioned-EDGE device, enables us to qualitatively compare the dynamic adsorption of emulsifiers with extremely distinct properties – SDS and proteins –, at rather relevant bulk concentrations (Sahin et al., 2016; Yasuno et al., 2004; Kukizaki & Goto, 2007).

To summarise, we studied emulsifier adsorption and its roles on the formation and instant coalescence of bubbles (and droplets) formed at time scales down to tens of microseconds, which are relevant to bubble (and droplet) formation during large-scale production, such as 0.1–30 ms in high-pressure homogenisers and 0.1–100 ms in colloid mills (Schultz, Wagner, Urban, & Ulrich, 2004). Our partitioned-EDGE device proves to be an useful platform for the characterisation and selection of emulsifiers for specific applications.

Credit authorship contribution statement

Boxin Deng: Methodology, Data curation, Investigation, Formal analysis, Visualization, Writing – original draft. **Karin Schroën:** Methodology, Supervision, Writing – review & editing. **Jolet de Ruiter:** Methodology, Supervision, Writing – review & editing.

Declaration of competing interest

The authors declare no conflicts of interest.

Data availability

Data will be made available on request.

Acknowledgement

The authors would like to thank the China Scholarship Council (grant number 201806790006) and FrieslandCampina for financial support.

Appendix A. Supplementary data

Supplementary data to this article can be found online at https://doi.org/10.1016/j.foodhyd.2023.108663.

References

Berry, J. D., Neeson, M. J., Dagastine, R. R., Chan, D. Y. C., & Tabor, R. F. (2015). Measurement of surface and interfacial tension using pendant drop tensiometry. *Journal of Colloid and Interface Science, 454*, 226–237. https://doi.org/10.1016/j.jcis.2015.05.012

Chen, Y., Narayan, S., & Dutcher, C. S. (2020). Phase-dependent surfactant transport on the microscale: Interfacial tension and droplet coalescence. *Langmuir, 36*(49), 14904–14923. https://doi.org/10.1021/acs.langmuir.0c02476

Crestel, E., Derzsi, L., Bartolomei, H., Bibette, J., & Bremond, N. (2019). Emulsification with rectangular tubes. *Physical Review Fluids, 4*(7), Article 073602. https://doi.org/10.1103/physrevfluids.4.073602

Dabestani, M., Yeganehzad, S., Krzan, M., & Miller, R. (2019). Characterisation of egg white adsorption layers under equilibrium and dynamic conditions. *Colloids and Surfaces A: Physicochemical and Engineering Aspects, 568*, 29–35. https://doi.org/10.1016/j.colsurfa.2019.01.066

De Jongh, H. H. J., Kosters, H. A., Kudryashova, E., Meinders, M. B. J., Trofimova, D., & Wierenga, P. A. (2004). Protein adsorption at air-water interfaces: A combination of details. *Biopolymers, 74*(1–2), 131–135. https://doi.org/10.1002/bip.20036

Deng, B., Schroën, K., & De Ruiter, J. (2021). Effects of dynamic adsorption on bubble formation and coalescence in partitioned-EDGE devices. *Journal of Colloid and Interface Science, 602*, 316–324. https://doi.org/10.1016/j.jcis.2021.06.014

Deng, B., Schroën, K., & De Ruiter, J. (2022). Dynamics of bubble formation in spontaneous microfluidic devices: Controlling dynamic adsorption via liquid phase properties. *Journal of Colloid and Interface Science, 622*, 218–227. https://doi.org/10.1016/j.jcis.2022.04.115

Deng, B., Schroën, K., & De Ruiter, J. (2023). Onsite coalescence behavior of whey protein-stabilized bubbles generated at parallel microscale pores: Role of pore geometry and liquid phase properteis. *Food Hydrocollods, 138*, 108435. https://doi.org/10.1016/j.foodhyd.2022.108435

Gao, T., & Rosen, M. J. (1995). Dynamic surface tension of aqueous surfactant solutions: 7. Physical significance of dynamic parameters and the induction period. *Journal of Colloid and Interface Science, 172*(1), 242–248. https://doi.org/10.1006/jcis.1995.1248

Giménez-Ribes, G., Sagis, L. M. C., & Habibi, M. (2020). Interfacial viscoelasticity and aging effect on droplet formation and breakup. *Food Hydrocolloids, 103*. https://doi.org/10.1016/j.foodhyd.2019.105616

Graham, D. E., & Phillips, M. C. (1979). Proteins at liquid interfaces: I Kinetics of adsorption and surface denaturation. *Journal of Colloid and Interface Science, 70*(3), 403–414. https://doi.org/10.1016/0021-9797(79)90048-1

Hinderink, E. B. A., Kaade, W., Sagis, L., Schroën, K., & Berton-Carabin, C. C. (2020). Microfluidic investigation of the coalescence susceptibility of pea protein-stabilised emulsions: Effect of protein oxidation level. *Food Hydrocolloids, 102*. https://doi.org/10.1016/j.foodhyd.2019.105610

Hinderink, E. B. A., Ruiter, J. De, Leeuw, J. De, Schro, K., Leonard, M., Sagis, C., et al. (2021). Early film formation in protein-stabilised emulsions : Insights from a microfluidic approach. *Food Hydrocolloids, 118*. https://doi.org/10.1016/j.foodhyd.2021.106785

Jafari, S. M., Assadpoor, E., He, Y., & Bhandari, B. (2008). Re-coalescence of emulsion droplets during high-energy emulsification. *Food Hydrocolloids, 22*(7), 1191–1202. https://doi.org/10.1016/j.foodhyd.2007.09.006

Joseph, F. Z. (1997). *Functionality of proteins in food*. Springer science & business media.

Kalli, M., Chagot, L., & Angeli, P. (2022). Comparison of surfactant mass transfer with drop formation times from dynamic interfacial tension measurements in microchannels. *Journal of Colloid and Interface Science, 605*, 204–213. https://doi.org/10.1016/j.jcis.2021.06.178

Kinoshita, K., Parra, E., & Needham, D. (2017). Adsorption of ionic surfactants at microscopic air-water interfaces using the micropipette interfacial area-expansion method : Measurement of the diffusion coefficient and renormalization of the mean ionic activity for SDS. *Journal of Colloid and Interface Science, 504*, 765–779. https://doi.org/10.1016/j.jcis.2017.05.077

Kovalchuk, N. M., Nowak, E., & Simmons, M. J. H. (2016). Effect of soluble surfactants on the kinetics of thinning of liquid bridges during drops formation and on size of satellite droplets. *Langmuir, 32*(20), 5069–5077. https://doi.org/10.1021/acs.langmuir.6b01467

Kovalchuk, N. M., Nowak, E., & Simmons, M. J. H. (2017). Kinetics of liquid bridges and formation of satellite droplets: Difference between micellar and bi-layer forming solutions. *Colloids and Surfaces A: Physicochemical and Engineering Aspects, 521*, 193–203. https://doi.org/10.1016/j.colsurfa.2016.08.060

Kukizaki, M., & Goto, M. (2007). Spontaneous formation behavior of uniform-sized microbubbles from Shirasu porous glass (SPG) membranes in the absence of water-phase flow. *Colloids and Surfaces A: Physicochemical and Engineering Aspects, 296*(1–3). https://doi.org/10.1016/j.colsurfa.2006.09.042

Liang, X., Li, M., Wang, K., & Luo, G. (2022). Determination of time-evolving interfacial tension and ionic surfactant adsorption kinetics in microfluidic droplet formation process. *Journal of Colloid and Interface Science, 617*, 106–117. https://doi.org/10.1016/j.jcis.2022.02.139

Mi, S., Fu, T., Zhu, C., Jiang, S., & Ma, Y. (2019). Mechanism of bubble formation in step-emulsification devices. *AIChE Journal, 66*, Article 16777. https://doi.org/10.1002/aic.16777

Mitropoulos, V., Mütze, A., & Fischer, P. (2014). Mechanical properties of protein adsorption layers at the air/water and oil/water interface: A comparison in light of the thermodynamical stability of proteins. *Advances in Colloid and Interface Science, 206*, 195–206. https://doi.org/10.1016/j.cis.2013.11.004

Muijlwijk, K., Colijn, I., Harsono, H., Krebs, T., & Berton-Carabin, C. (2017). Coalescence of protein-stabilised emulsions studied with microfluidic. *Food Hydrocolloids, 70*, 94–104. https://doi.org/10.1016/j.foodhyd.2017.03.031

Muijlwijk, K., Hinderink, E., Ershov, D., Berton-Carabin, C., & Schroën, K. (2016). Interfacial tension measured at high expansion rates and within milliseconds using microfluidics. *Journal of Colloid and Interface Science, 470*, 71–79. https://doi.org/10.1016/j.jcis.2016.02.041

Narsimhan, G., & Xiang, N. (2018). Role of proteins on formation, drainage, and stability of liquid food foams. *Annual Review of Food Science and Technology, 9*(1), 45–63. https://doi.org/10.1146/annurev-food-030216-030009

Roché, M., Aytouna, M., Bonn, D., & Kellay, H. (2009). Effect of surface tension variations on the pinch-Off behavior of small fluid drops in the presence of surfactants. *Physical Review Letters, 103*(26), 1–4. https://doi.org/10.1103/PhysRevLett.103.264501

Sahin, S., Bliznyuk, O., Rovalino Cordova, A., & Schroën, K. (2016). Microfluidic EDGE emulsification: The importance of interface interactions on droplet formation and pressure stability. *Scientific Reports, 6*. https://doi.org/10.1038/srep26407

Saito, M., Yin, L. J., Kobayashi, I., & Nakajima, M. (2005). Preparation characteristics of monodispersed oil-in-water emulsions with large particles stabilized by proteins in straight-through microchannel emulsification. *Food Hydrocolloids, 19*(4), 745–751. https://doi.org/10.1016/j.foodhyd.2004.08.005

Schultz, S., Wagner, G., Urban, K., & Ulrich, J. (2004). High-pressure homogenization as a process for emulsion formation. *Chemical Engineering & Technology, 27*(4), 361–368. https://doi.org/10.1002/ceat.200406111

Stoffel, M., Wahl, S., Lorenceau, E., Höhler, R., Mercier, B., & Angelescu, D. E. (2012). Bubble production mechanism in a microfluidic foam generator. *Physical Review Letters, 108*(19), Article 198302. https://doi.org/10.1103/PhysRevLett.108.198302

Sugiura, S., Nakajima, M., Iwamoto, S., & Seki, M. (2001). Interfacial tension driven monodispersed droplet formation from microfabricated channel array. *Langmuir, 17*(18), 5562–5566. https://doi.org/10.1021/la010342y

Sugiura, S., Nakajima, M., Oda, T., Satake, M., & Seki, M. (2004). Effect of interfacial tension on the dynamic behavior of droplet formation during microchannel emulsification. *Journal of Colloid and Interface Science, 269*(1), 178–185. https://doi.org/10.1016/j.jcis.2003.07.031

Tadros, T. F. (2013). Emulsion formation, stability, and rheology. In *Emulsion Formation and stability*. Wiley-VCH Verlag GmbH & Co. KGaA. https://doi.org/10.1002/9783527647941.

Tcholakova, S., Denkov, N. D., & Lips, A. (2008). Comparison of solid particles, globular proteins and surfactants as emulsifier. *Physical Chemistry Chemical Physics, 10*(48), 1608–1627. https://doi.org/10.1039/b705094a

Van Dijke, K. C., Schroën, K., van der Padt, A., & Boom, R. (2010). EDGE emulsification for food-grade dispersions. *Journal of Food Engineering, 97*(3), 348–354. https://doi.org/10.1016/j.jfoodeng.2009.10.028

Vladisavljevi, G. T., Kobayashi, I., & Nakajima, M. (2008). Generation of highly uniform droplets using asymmetric microchannels fabricated on a single crystal silicon plate : Effect of emulsifier and oil types. *Powder Technology, 183*, 37–45. https://doi.org/10.1016/j.powtec.2007.11.023

Walstra, P., Wouters, J. T. M., & Geurts, T. J. (2005). *Dairy science and technology*. CRC. https://doi.org/10.1201/9781420028010

Wang, K., Lu, Y. C., Xu, J. H., & Luo, G. S. (2009). Determination of dynamic interfacial tension and its effect on droplet formation in the T-shaped microdispersion process. *Langmuir, 25*(4), 2153–2158. https://doi.org/10.1021/la803049s

Wang, X., Riaud, A., Wang, K., & Luo, G. (2015). Pressure drop-based determination of dynamic interfacial tension of droplet generation process in T-junction microchannel. *Microfluidics and Nanofluidics, 18*(3), 503–512. https://doi.org/10.1007/s10404-014-1449-0

Wang, K., Xu, J., Liu, G., & Luo, G. (2015). Role of interfacial force on multiphase microflow — an important meso-scientific issue. In *Advances in Chemical Engineering* (1st ed., Vol. 47). Elsevier Inc. https://doi.org/10.1016/bs.ache.2015.10.003.

Wang, K., Zhang, L., Zhang, W., & Luo, G. (2016). Mass-transfer-controlled dynamic interfacial tension in microfluidic emulsification processes. *Langmuir, 32*(13), 3174–3185. https://doi.org/10.1021/acs.langmuir.6b00271

Xu, J. H., Dong, P. F., Zhao, H., Tostado, C. P., & Luo, G. S. (2012). The dynamic effects of surfactants on droplet formation in coaxial microfluidic devices. *Langmuir, 28*(25), 9250–9258. https://doi.org/10.1021/la301363d

Yasuno, M., Sugiura, S., Iwamoto, S., Nakajima, M., Shono, A., & Satoh, K. (2004). Monodispersed microbubble formation using microchannel technique. *AIChE Journal, 50*(12), 3227–3233. https://doi.org/10.1002/aic.10276

Zhu, P., & Wang, L. (2017). Passive and active droplet generation with microfluidics : A review. *Lab on a Chip, 17*, 34–75. https://doi.org/10.1039/C6LC01018K